Journal of Materials Chemistry A

PAPER

Check for updates

Cite this: J. Mater. Chem. A, 2017, 5, 7355

Charting the relationship between phase type-surface area-interactions between the constituent atoms and oxygen reduction activity of Pd–Cu nanocatalysts inside fuel cells by *in operando* high-energy X-ray diffraction†

Yazan Maswadeh,[a] Shiyao Shan,[b] Binay Prasai,[a] Yinguang Zhao,[b] Zhi-Hui Xie,[b] Zhipeng Wu,[b] Jin Luo,[b] Yang Ren,[c] Chuan-Jian Zhong *[b] and Valeri Petkov *[a]

The activity and stability of nanoalloy catalysts for chemical reactions driving devices for clean energy conversion, in particular the oxygen reduction reaction (ORR), depend critically on optimizing major structural characteristics of the nanoalloys, such as the phase composition, surface area and bonding interactions between the constituent atoms, for the harsh operating conditions inside the devices. The effort requires good knowledge of the potential effect of changes in these characteristics on the catalytic functionality of the nanoalloys and, hence, on the devices' performance. We present the results from an *in operando* high-energy X-ray diffraction (HE-XRD) study on the concurrent changes in the structural characteristics and ORR activity of Pd–Cu nanoalloy catalysts as they function at the cathode of a proton exchange membrane fuel cell (PEMFC). We find that the as-prepared Pd–Cu nanoalloys with a chemical composition close to Pd_1Cu_1 are better ORR catalysts in comparison with Pd_1Cu_2, *i.e.* Pd-poor, and Pd_3Cu_1, *i.e.* Pd-rich, nanoalloys. Under operating conditions though, the former suffers a big loss in ORR activity appearing as a slow-mode oscillation in the current output of the PEMFC. Losses in ORR activity suffered by the latter also exhibit sudden drops and rises during the PEMFC operation. Through atomic pair distribution function (PDF) analysis of the *in operando* HE-XRD data, we identify the structural changes of Pd–Cu alloy NPs that are behind the peculiar decay of their ORR activity. The results uncover the instant link between the ever-adapting structural state of ORR nanocatalysts inside an operating PEMFC and the performance of the PEMFC. Besides, our results indicate that, among others, taking control over the intra-particle diffusion of metallic species in nanoalloy catalysts may improve the performance of PEMFCs significantly and, furthermore, *in operando* HE-XRD can be an effective tool to guide the effort. Finally, we argue that, though showing less optimal ORR activity in the as-prepared state, monophase Pd–Cu alloy catalysts with a composition ranging between Pd_1Cu_1 and Pd_3Cu_1 may deliver optimal performance inside operating PEMFCs.

Received 20th January 2017
Accepted 20th March 2017

DOI: 10.1039/c7ta00688h

rsc.li/materials-a

Introduction

Devices for clean energy conversion such as proton exchange membrane fuel cells (PEMFCs) are a very promising technology for meeting the ever-increasing global energy demand.[1,2] A major obstacle on the road to the commercialization of PEMFCs is the lack of affordable, highly active and sufficiently stable catalysts for the sluggish oxygen reduction reaction (ORR) taking place at the PEMFC cathode.[3–6] Without loss of generality, the reaction can be expressed as $O_2 + 4H^+ + 4e^- \rightarrow H_2O$, that is, oxygen molecules adsorbed and reduced at the PEMFC cathode react with protons supplied by the PEMFC anode to form water. Though the exact mechanism of the ORR is still under debate, there is strong experimental evidence that the ORR over a catalytic site proceeds *via* a number of elementary steps involving, among others, a cleavage of the strong O–O bond in molecular oxygen and removal of reaction intermediates such as atomic oxygen and hydroxyl (OH) groups. Generally, it is believed that an efficient catalyst for the ORR would bind oxygen molecules with ample strength to allow the cleavage of O–O bonds but weakly enough to liberate the

[a]Department of Physics, Central Michigan University, Mt. Pleasant, Michigan 48898, USA. E-mail: petko1vg@cmich.edu

[b]Department of Chemistry, State University of New York at Binghamton, Binghamton, New York 13902, USA. E-mail: cjzhong@binghamton.edu

[c]X-ray Science Division, Advanced Photon Source, Argonne National Laboratory, Argonne, Illinois 60439, USA

† Electronic supplementary information (ESI) available. CCDC. For ESI and crystallographic data in CIF or other electronic format. See DOI: 10.1039/c7ta00688h

reaction intermediates and product when the reaction ends. In addition, it is believed that the binding energy of atomic oxygen can serve as an indicator for catalytic activity for the ORR.[7–9]

Pure Pt is the best monometallic catalyst for the ORR, even though, according to theory, it binds oxygen a bit too strongly by about 0.2 eV.[10,11] For comparison, 3d-transition metals (TMs) such as Cu and Ni bind oxygen from 0.5 eV to 1 eV stronger than Pt does it. Hence, under typical ORR conditions, their surface would oxidize fast thus becoming unreactive. On the other hand, the binding energy of oxygen on some noble metals (NMs) such as Au is about 1.5 eV smaller than that on Pt. For these metals the cleavage of O–O bonds, that is the dissociation of adsorbed O_2 molecules, would render the ORR kinetics slow.[12] Unfortunately, though exhibiting an excellent ORR activity, pure Pt is not suitable for large-scale applications largely because it is one of the world's rarest metals. The same pertains to Pt nanoparticles (NPs). The problem has been addressed by numerous studies and NPs of the NM–TM alloy family, where NM = Pt, Pd and Au and TM = Ni, Co, Fe, Cu, V and Mo, have been found both more affordable and active catalyst for the ORR as compared to pure Pt NPs.[13–17] Note, following the widely adopted definition,[18] here we use the term "alloy" to describe any mixture of distinct metallic species, irrespective of the degree of their mixing and way of mixing. Despite the progress made, PEMFCs are not on the market yet for the NM–TM nanoalloy catalysts would fail to function as expected inside operating PEMFCs thus severely limiting their performance. The failure is because under the highly corrosive conditions at the PEMFC cathode, NM–TM alloy NPs undergo specific atomic-scale changes that inflict substantial losses in their ORR activity. The changes can occur simultaneously and on largely different length-scales, ranging from sub-Å fluctuations in the positions of atoms inside individual NPs and local nanophase transformations to nm-sized growth involving effective mass transport across the PEMFC cathode.[19–21] As such, the changes can be difficult to disentangle and so rank in terms of contribution to the undue ORR activity losses when NM–TM NPs are studied outside operating PEMFCs, *i.e. ex situ*. One of the reasons is that, typically, *ex situ* studies are done within timeframes that do not necessarily fit well the dynamics of the atomic-scale changes of NM–TM alloy NPs during PEMFCs' operation.[22] Besides, NM–TM alloy NPs exposed to the gas-phase environment inside operating PEMFCs do not necessarily follow the trajectory of structural changes experienced by NM–TM NPs exposed to the liquid phase environment inside laboratory electrochemical cells.[23]

When aiming at improving the functionality of NM–TM alloy NPs as ORR catalysts for PEMFCs, it is important to assess accurately both the atomic-scale changes and decay of the ORR activity of the NPs taking place during the PEMFC operation, establish their relationship and then use it to design a strategy for reducing the latter through taking control over the former. In addition, it is important to use a probe that does not disturb the NPs during the PEMFC operation.[24–27] Here we employ high-energy X-ray diffraction (HE-XRD) to probe the concurrent evolution of major structural characteristics, such as the nanophase type, surface area and interactions between the constituent atoms, and ORR activity of three members of the family of Pd–Cu nanoalloy catalysts with a composition close to Pd_1Cu_2, Pd_1Cu_1 and Pd_3Cu_1, as they function at the cathode of an actual PEMFC. It is to be noted that, recently, Pd alloyed with TMs, in particular Cu, has been actively pursued as a low-cost alternative to Pt-based catalysts for the ORR, alcohol and formic acid oxidation, low-temperature oxidation of CO, and other reactions of technological and environmental importance.[28–31] We analyze the *in operando* HE-XRD data in terms of atomic pair distribution functions (PDFs) and find that Pd–Cu alloy NPs wherein the concentration of Pd species $\leq$50%, *i.e.* Pd_1Cu_2 and Pd_1Cu_1 NPs, are composed of a bcc-type core and fcc-type shell. On the other hand, Pd–Cu alloy NPs rich in Pd, *i.e.* Pd_3Cu_1 alloy NPs, appear as a single fcc-type nanophase. Also, we find that the as-synthesized Pd_1Cu_1 NPs are superior to both Pd-poor (Pd_1Cu_2) and Pd-rich (Pd_3Cu_1) NPs with regard to catalytic activity for the ORR. Under actual operating conditions though, the former appears less stable at an atomic scale and so suffer a larger loss in ORR activity as compared to the latter. Notably, we find that bonding interactions between atoms in Pd–Cu alloy NPs relax significantly and so the ORR activity of the NPs drops irreversibly soon after the PEMFC starts operating. Changes in the nanophase composition of the NPs also contribute to that drop. On the other hand, the gradual growth of the NPs during the PEMFC operation and the related loss in surface area become a factor contributing significantly to the loss in ORR activity only after the PEMFC has operated for a while. Hence, we argue that efforts to produce Pd–Cu alloy NPs that are both highly active and stable catalysts for the ORR in PEMFCs should aim at restraining not only the NP growth involving exchange of atomic species between individual NPs but also the local atomic relaxation and nanophase fluctuations within the NPs involving mere intra-particle diffusion of Cu and Pd atoms. Also, we argue that, though showing less optimal ORR activity in the as-prepared state, monophase Pd–Au alloy catalysts with a composition ranging between Pd_1Cu_1 and Pd_3Cu_1 may deliver optimal performance inside operating PEMFCs.

Experimental

Pd–Cu alloy NPs were synthesized following a wet chemistry route described in the Methods section of the ESI.† The as-synthesized NPs were deposited on carbon black and activated for catalytic applications by a post-synthesis treatment involving heating at 260 °C in N_2 for 30 min followed by heating at 400 °C in 15 vol% H_2 for 120 min.

The overall chemical composition of activated Pd–Cu alloy NPs, hereafter referred to as fresh Pd–Cu NPs, and Pd–Cu NPs used as ORR catalysts inside an operating PEMFC was determined by inductively coupled plasma atomic emission spectroscopy (ICP-AES). Measurements were done on a Perkin Elmer 2000 DV ICP-OES instrument. As desired, fresh Pd–Cu alloy NPs appeared with an overall chemical composition close to Pd_1Cu_2, Pd_1Cu_1 and Pd_3Cu_1, that is, $Pd_{34}Cu_{66}$, $Pd_{51}Cu_{49}$ and $Pd_{75}Cu_{25}$, respectively. Upon undergoing 1450 potential cycles between 0.6 V and 1.2 V inside an PEMFC, the overall chemical composition of the NPs changed to $Pd_{43}Cu_{57}$, $Pd_{61}Cu_{39}$ and $Pd_{78}Cu_{22}$,

respectively. Evidently, due to their relatively low reduction potential (0.337 V for Cu *vs.* 0.987 V for Pd) and the corrosive conditions at the PEMFC cathode, Cu species have leached from the Pd–Cu alloy NPs during the PEMFC operation. $Pd_{34}Cu_{66}$ and $Pd_{51}Cu_{49}$ alloy NPs though have suffered a larger loss in Cu species as compared to $Pd_{75}Cu_{25}$ NPs. In line with the results of others, our data indicate that, when in clear majority, Pd (NM) species in Pd(NM)–Cu(TM) protect the minority Cu (TM) species from dissolution to a certain degree.[3,20,33–35]

The size and shape of fresh Pd–Cu alloy NPs were determined by Transmission Electron Microscopy (TEM) on a JEM-2200FS instrument operated at 200 kV. Exemplary TEM and high-resolution (HR)-TEM images are summarized in Fig. S1.† As can be seen in the figure, the NPs are approximately 5.1 (±0.5) nm in size, spherical in shape and with fairly low dispersity. In addition, the NPs possess a good degree of crystallinity as indicated by the clear lattice fringes appearing in the respective HR-TEM images. The size of the NPs was also determined from the full width at the half maximum (FWHM) of strong Bragg-like peaks in the respective HE-XRD patterns shown in Fig. 1. Within the limits of the experimental accuracy, XRD and TEM determined sizes of fresh Pd–Cu NPs appeared about the same.

The near surface electronic structure and chemical composition of fresh Pd–Cu NPs were determined by X-ray photoelectron spectroscopy (XPS). Note, though soft X-rays used in XPS can penetrate a substantial distance into metallic NPs, the XPS signal diminishes exponentially with that distance. Hence, XPS is much more sensitive to the near surface area than to the interior of metallic NPs. Measurements were carried out on a Physical Electronics Quantum 2000 scanning ESCA microprobe equipped with a focused monochromatic Al Kα X-ray (1486.7 eV) source, a spherical analyser and a 16-element multichannel detector. The binding energy (BE) scale of the instrument was calibrated using C 1s peak at 284.8 eV, Cu $2p_{3/2}$ peak at 932.7 eV and Au $4f_{7/2}$ peak at 83.96 eV as internal standards. The percentages of individual atomic species near the NP surface were determined by analysing the area of the respective XPS peaks. Exemplary XPS spectra of fresh Pd–Cu NPs are shown in Fig. S2.† As can be seen in the figure, the Cu $2p_{3/2}$ core-level peak position in Pd_xCu_{100-x} alloy NPs (x = 34, 51, 75) is shifted by −0.41 eV, −0.5 eV and −0.82 eV,

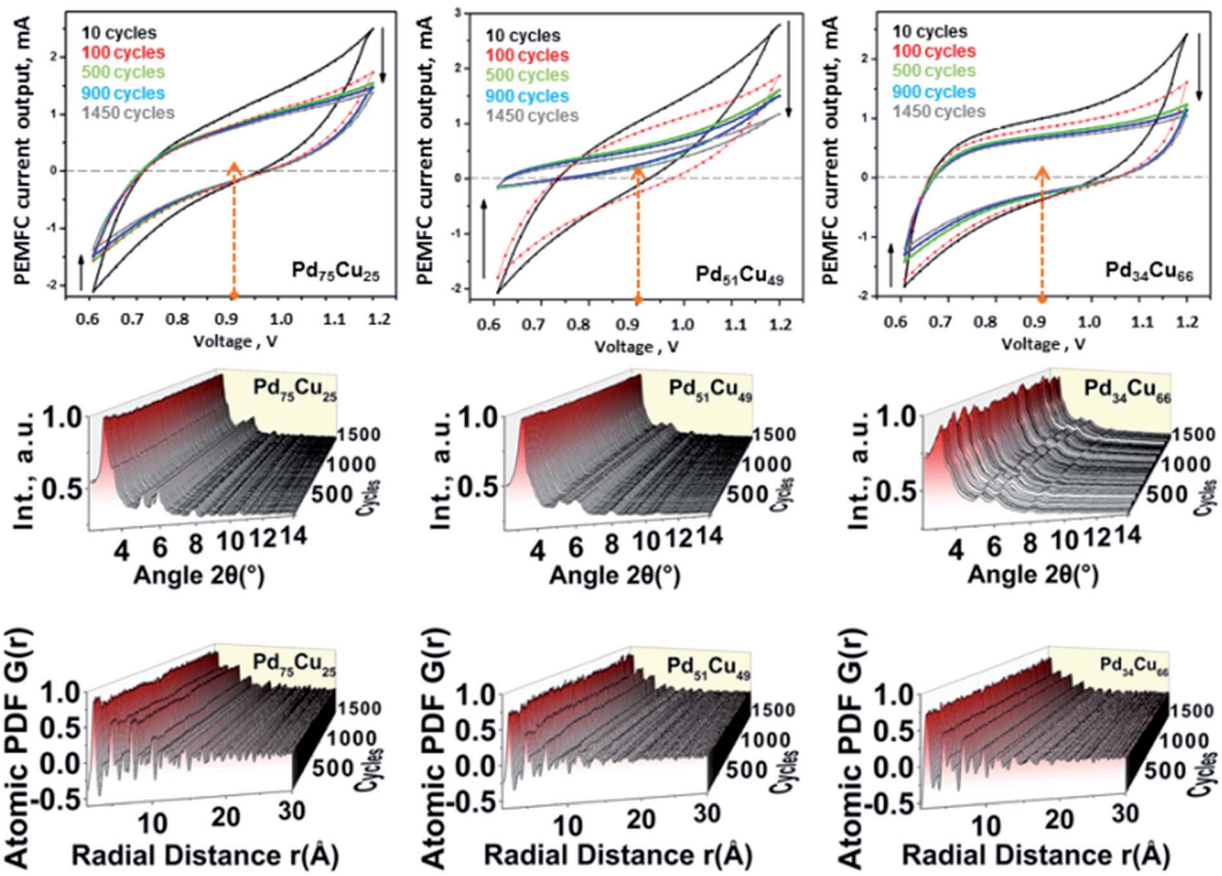

Fig. 1 (First row) Selected polarization curves representing the PEMFC current output recorded during 1450 potential cycles in the range from 0.6 V to 1.2 V. The curves tend to collapse, *i.e.* the current diminishes during the PEMFC operation, as emphasized by the vertical black arrows. That is because under actual operating conditions, the PEMFC cathode catalyst, *i.e.* Pd–Cu alloy NPs, suffer substantial loss in ORR activity. Following the protocol of *ex situ* catalytic studies, the current output of the PEMFC at 0.9 V on the polarization curves (follow the orange vertical arrows) is used as a measure of the effective MA of Pd–Cu NPs for the ORR.[4,12,75] The so-obtained MA values are summarized in Fig. S5.† Also, for completeness, all polarization curves are summarized in Fig. S16.† (Second row) *In operando* HE-XRD patterns of Pd–Cu NPs as a function of the number of potential cycles. (Third row) Atomic PDFs of Pd–Cu NPs derived from the respective *in operando* HE-XRD patterns.

respectively, in comparison to the bulk value of 932.7 eV. As can also be seen in the figure, the Pd $3d_{3/2}$ core-level peak position in the NPs is shifted by −0.07 eV, −0.1 eV and −0.19 eV, respectively, in comparison to the bulk value of 340.7 eV. The shifts and their systematic change with the Pd concentration indicate that Pd and Cu atoms in the NPs strongly interact with each other, *i.e.* alloy.[36] Independent EXAFS studies have also indicated that Pd and Cu tend to interact strongly when intermixed at the nanoscale.[37] In the framework of the electronegativity principle, upon alloying, charge would be expected to flow from Cu to Pd atoms because the latter is more electronegative (2.2) than the former (1.9). However, a simple charge transfer model cannot explain the same sign of Cu $2p_{3/2}$ and Pd $3d_{3/2}$ core-level shifts in Pd–Cu alloy NPs.[38] Other factors such as the particular bimetallic composition, details in the synthesis and post-synthesis treatment, changes in the geometry of the first coordination sphere, nanophase type, and others, have to be accounted for.[39] The XPS determined near-surface composition of fresh Pd_xCu_{100-x} alloy NPs (x = 34, 51, 75) turned out to be "$Pd_{39}Cu_{61}$", "$Pd_{58}Cu_{42}$" and "$Pd_{81}Cu_{19}$", respectively. Evidently, regardless the surface energy of Pd (2.05 J m^{-2}) being higher than that of Cu (1.85 J m^{-2}), the near-surface region of fresh Pd–Cu alloy NPs appeared somewhat Pd-enriched. As discussed in the work of others, when within certain limits, the latter would enhance the catalytic activity and stability of Pd–Cu alloy NPs for the ORR under the acidic conditions inside PEMFCs.[32,40–44]

The catalytic activity of fresh Pd–Cu alloy NPs for the ORR was determined by cyclic voltammetry (CV) and rotating disk electrode (RDE) experiments carried out on a standard 3-electrode electrochemical cell at room temperature. The electrolyte in the cells (0.1 M $HClO_4$) was de-aerated with high purity N_2 before the CV experiments. For the RDE experiments, the electrolyte was saturated with O_2. Data of the electrochemical active surface area (ECSA), mass activity (MA) and specific activity (SA) of fresh Pd–Cu NPs for the ORR are summarized in Table S1.† Data show that fresh $Pd_{51}Cu_{49}$ alloy NPs are superior to fresh Pd-poor ($Pd_{34}Cu_{66}$) and Pd-rich ($Pd_{75}Cu_{25}$) NPs in terms of both MA and SA for the ORR.

An actual PEMFC optimized for HE-XRD experiments was used to assess the catalytic functionality of Pd_xCu_{100-x} alloy NPs (x = 34, 51, 75) for the ORR under actual operating conditions. The schematic of the PEMFC is shown in Fig. S3.† Membrane electrode assemblies (MEAs) for the PEMFC were prepared as described in the Methods section of the ESI.† The PEMFC was cycled between 0.6 and 1.2 V for about 5 h (1450 cycles) following a protocol recommended by DOE.[12] During the cycling, high purity hydrogen and nitrogen gas were fed to the PEMFC anode and cathode compartments, respectively. Pure Pt NPs were used as the PEMFC anode (hydrogen oxidation reaction) catalyst and Pd–Cu alloy NPs were used as the PEMFC cathode (ORR) catalyst. The current output of the PEMFC was non-stop recorded during the voltage cycling. Selected polarization curves showing the current output of the PEMFC resulting from the repetitive application of external voltages are shown in Fig. 1. The curves are typical for accelerated tests for activity and stability of NM–TM nanoalloy catalysts for the ORR (*e.g.* see Fig. 2 in ref. 45).

Atomic-level changes in Pd–Cu alloy NPs functioning as ORR catalysts at the cathode of the PEMFC were probed by HE-XRD. Experiments were done at the 11-ID-C beamline of the Advanced Photon Source at the Argonne National Laboratory using X-rays with an energy of 115 keV (λ = 0.1080 Å) and a large area detector (41 cm × 41 cm amorphous Si flat panel detector made by Perkin Elmer; see Fig. S3†). HE-XRD patterns were collected in intervals of 3 min, for 1 min each, throughout the PEMFC operation (potential cycling). HE-XRD data of the PEMFC with a MEA containing the anode catalyst alone were taken separately and used to correct the HE-XRD patterns of Pd–Cu NPs taken during the PEMFC operation, as exemplified in Fig. S17.† Experimental *in operando* HE-XRD patterns of Pd_xCu_{100-x} alloy NPs (x = 34, 51, 75), as corrected for the PEMFC hardware and other background-type (air, *etc.*) scattering, are shown in Fig. 1. As can be seen in the figure, the HE-XRD patterns exhibit a few strong Bragg-like peaks at low diffraction angles and almost no sharp features at high diffraction angles, *i.e.* are rather diffuse in nature. This rendered the well-established, sharp Bragg peaks-based procedures for characterizing the atomic-scale structure of bulk metals and alloys difficult to apply to the NPs studied here. Therefore, the diffuse *in operando* HE-XRD patterns were analysed in terms the so-called atomic pair distribution functions (PDFs) which have proven very useful in structure studies of metallic NPs.[32,46,47] The PDFs are shown in Fig. 1. More details of the derivation of the atomic PDFs and their interpretation can be found in the Methods section of the ESI.† Here it is to be underlined that experimental HE-XRD patterns and so their Fourier counterparts, the atomic PDFs, reflect ensemble averaged structural features of all metallic NPs sampled by the X-ray beam in a way traditional powder XRD patterns reflect ensemble averaged structural features of all polycrystallites sampled by the X-ray beam in those experiments. Using NP ensemble averaged structural features to understand and explain NP ensemble averaged properties (*e.g.* catalytic, magnetic, optical, *etc.*) puts the exploration of atomic-scale structural characteristics and properties of metallic NPs on the same footing.

Discussion

Among all other late-TMs, Pd can be considered as the most Pt-like metal in terms of catalytic properties. The binding of oxygen species to Pd though is about 0.3 eV stronger than optimal and so pure Pd catalysts lack sufficient ORR activity. Remarkably, although pure Cu binds oxygen species stronger than both Pd and Pt, studies have shown that adding Cu to Pd would result in alloy catalysts with improved ORR activity in comparison to pure Pd.[32,33,48,49] In general, the improved ORR activity of NM–TM alloy NPs is attributed to one or more of the following factors: (i) ligand/electronic effects arising from charge transfer between TM and NM atoms,[8,10,17] (ii) strain effects arising from the difference between the size of NM and TM atoms[8,50–52] and (iii) geometric effects where a particular number and configuring of nearby surface NM and TM atoms are needed for the ORR reaction to persist.[53–55]

Studies have suggested that nearby surface Pd and Cu atoms in Pd–Cu alloy NPs are likely to exchange charge, including

strong hybridization between Pd 4d and Cu 3d orbitals, because of the significant energy overlap of the d-bands of Pd and Cu.[40,56] Furthermore, the studies suggested that the charge exchange would increase the filling of the d-band of Pd and so its energy position would shift downwards with respect to the Fermi energy in the NPs. On the other hand, the average d-band level of surface Cu atoms would shift up in energy. Based on the d-band center theory on the catalytic properties of transition metals and alloys,[7,8] the studies concluded that, due to charge exchange effects, the Pd–O_{ads} binding energy would decrease gradually as the Cu concentration in Pd–Au alloy NPs increases towards 50%, thereby significantly increasing the catalytic activity of the NPs for the ORR. At high Cu concentrations though, the binding of oxygen species onto the NPs would be dominated by the strong Cu–O interactions and so the ORR activity of the NPs would drop, as observed by experiment. Recent DFT studies concluded that the interrelated lowering of the energy barrier for O_2 dissociation and weakening of the adsorption strength of O, OH, and OOH species induced by Cu → Pd charge transfer are indeed responsible for the superb ORR activity exhibited by Pd_xCu_{100-x} alloy NPs with $x \sim 50\%$.[56] Considering the difference in the elemental size of Pd (2.76 Å) and Cu (2.56 Å) atoms, other studies have pointed out that Pd-involving bonding distances in Pd–Au alloy NPs would gradually shrink as the concentration of Cu in the NPs increases, for minimizing atomic-level stresses.[32,57–60] Furthermore, the studies argued that the shrinking of Pd-involving bonding distances in Pd–Cu alloy NPs would strengthen d electron–d electron interactions, broaden the d-band of surface Pd atoms and so its center would move downward with respect to the Fermi level in the NPs. The opposite would be true for the d-band of surface Cu atoms. Based on the d-band center theory, the studies concluded that, due to local strain effects, the overlap between d-orbitals of surface Pd atoms and 2p-orbitals of the adsorbed oxygen species would decrease and so the Pd–O_{ads} binding energy become just about optimal, rendering Pd_xCu_{100-x} alloy NPs with $x \sim 50\%$ superb catalysts for the ORR. The importance of surface Cu atoms as sites for O–O bond breaking and forming of O_{ads} species has also been emphasized. According to these studies, the concentration of surface Cu species in Pd–Cu alloy NPs should be close to 30% for the ORR to persist.[61–64] Altogether, studies conducted so far have indicated that the catalytic functionality of Pd–Cu alloy NPs is highly dependent on (i) their phase type, including the relative ratio and mutual distribution of the constituent Pd and Cu atoms with respect to each other, (ii) the strength of interactions between nearby Pd and Cu atoms, including charge exchange and changes in near-neighbor/bonding distances, and (iii) the availability of surface sites active for the ORR, including an optimum concentration of surface Cu atoms. Hence, to reveal the atomic-level changes of Pd–Cu alloy NPs that contribute the most to the decay of their ORR activity, we concentrated on determining the evolution of the phase type, including the strength of interaction between the constituted atoms, and surface area of the NPs as a function of the potential cycles of the PEMFC. Note, according to Pauling's theory of chemical bonding,[65–67] and as shown by independent experimental[68] and DFT studies,[69] the length and strength of metal-to-metal atom bonds and charge exchange between the metal atoms involved in the bonds are intimately coupled and so difficult to tell apart. For that reason, we consider that strain and ligand effects in Pd–Cu NPs largely act together at an atomic level and refer to them as bonding effects. Also, in line with the work of others,[32,40,58,59] we use Pd-involving bonding distances as a measure of the bonding effects, *i.e.* strength of interactions between atoms in Pd–Cu alloy NPs.

It has been recognized that the large surface to volume ratio affects strongly the thermodynamic properties of metals and alloys confined to nanoscale dimensions and so can lead to a stabilization of particular nanophases at the expense of others. The nanophases can have novel functional properties such as, for example, unparalleled catalytic activity for the ORR. Furthermore, it has been recognized that under the constraint of a small particle size, the nanophases may not necessarily have bulk counterparts.[70,71] Hence, to determine the phase type of Pd_xCu_{100-x} alloy NPs (x = 34, 51, 75) we generated several plausible Pd–Cu nanophases including fcc Pd–Cu random alloy NPs, fcc Pd–Cu alloy NPs with a surface enriched in Pd, Janus-type Pd–Cu NPs, fcc Pd–Cu NPs with a surface enriched in Cu, bcc Pd–Cu alloy NPs, pure Cu core@Pd shell NPs, pure Pd core@Cu shell NPs, Pd–Cu–Pd sandwich type NPs and NPs whose core(interior) and shell(near surface region) are a bcc and fcc alloy enriched in Pd, respectively. The nanophases reflected both the structural diversity of Pd–Cu alloy NPs, as revealed by prior structure studies,[72] and the complex phase diagram of bulk Pd–Cu alloys, exhibiting coexisting chemically disordered and ordered face-centered-cubic (fcc)-type and body-centered-cubic (bcc)-type alloys.[73] Besides, to be as realistic as possible, the nanophases reflected the size, shape and chemical composition of Pd_xCu_{100-x} alloy NPs (x = 34, 51, 75) studied here, as determined by TEM, HR-TEM, ICP-AES and XPS experiments. Moreover, the nanophases were optimized in terms of energy, *i.e.* stabilized at atomic level, by Molecular Dynamics (MD) simulations described in the Methods section of the ESI.† The MD optimized nanophases are shown in Fig. S8–S10.† Atomic PDFs computed from the nanophases were matched against the experimental PDFs of Pd_xCu_{100-x} alloy NPs (x = 34, 51, 75), as exemplified in Fig. S11–S14,† and the actual nanophase type of the NPs was determined strictly following the "search and match"-type approach used in the "phase analysis" of bulk metals and alloys.[74]

The results of the "nanophase analysis" showed that fresh $Pd_{34}Cu_{66}$ and $Pd_{51}Cu_{49}$ NPs are composed of a bcc Pd–Cu core and fcc Pd–Cu shell rich in Pd. On the other hand, fresh $Pd_{75}Cu_{25}$ NPs were found to be an fcc Pd–Cu nanoalloy rich in Pd at the surface. The average Pd-involving bonding distances in the fresh Pd–Cu NPs, as estimated by the position of the peaks in the respective atomic PDFs, turned out to be 2.62 Å, 2.67 Å and 2.72 Å, that is, contracted by 5%, 3% and 1.5%, respectively, as compared to those in pure Pd (2.76 Å). Altogether, in line with the results of prior studies,[33,41] we found that Pd–Cu alloy NPs (i) with an overall composition close to Pd_1Cu_1, (ii) surface enriched in Pd (surface Pd concentration of 59% per XPS *vs.* average concentration of 51% per ICP-AES) and (iii)

a bcc-type core and fcc-type shell wherein the constituent atoms interact strongly and so the Pd-involving bonding distances are shrunk considerably (3%) are optimal catalysts for the ORR. On the other hand, Pd–Cu alloy NPs (i) with an overall composition close to Pd_1Cu_3 and Pd_3Cu_1 and (ii) constituent atoms interacting a bit too strongly and weakly leading to a very large (5%) and relatively small (1.5%) shrinking of Pd-involving bonding distances, respectively, are not optimal catalysts for the ORR. As shown by prior studies,[40,57–64] the rather high and low concentrations of surface Cu atoms in the former (61% per XPS) and latter (19% per XPS), respectively, would not be beneficial to ORR kinetics either.

Next, we considered the evolution of the ORR activity of Pd_xCu_{100-x} alloy NPs ($x = 34$, 51, 75) during the PEMFC operation as reflected by the evolution of the current output of the PEMFC exemplified in Fig. 1 and summarized in Fig. S15.† As can be seen in the figures, the polarization curves, that is the current output of the PEMFC *vs.* the applied external voltage, flatten out with the number of voltage cycles signalling the deteriorating performance of the PEMFC as the ORR at its cathode proceeds. Following the protocol of *ex situ* catalytic studies,[4,12,75] we designate the current output of the PEMFC at 0.9 V on the polarization curves as a measure of the effective MA of PEMFC cathode catalysts, *i.e.* Pd–Cu alloy NPs, for the ORR. The resulting MA values are summarized in Fig. S5.† Note, here we use the term "effective" to draw attention to the fact that MA values obtained on a standard 3-electrode cell and functioning PEMFC may exhibit similar trends but may not necessarily appear the same.[12,13,20]

As can be seen in the figure, the ORR activity of Pd_xCu_{100-x} alloy NPs ($x = 34$, 51, and 75) decays very fast within the first few hundred PEMFC cycles amounting to about 2 h of the PEMFC operation. Then, the decay becomes nearly gradual. The total loss in the ORR suffered by the different NPs though is significantly different. In particular, Pd–Cu NPs poor and rich in Pd, that is $Pd_{34}Cu_{66}$ and $Pd_{75}Cu_{25}$ NPs, suffered, respectively, 35% and 28% loss in ORR activity whereas the MA of $Pd_{51}Cu_{49}$ for the ORR dropped by 60% for 1450 potential cycles. Control experiments on the evolution of MA of $Pd_{51}Cu_{49}$ alloy NPs for the ORR during potential cycling inside a standard 3-electrode cell showed that, regardless the experimental conditions, $Pd_{51}Cu_{49}$ alloy NPs tend to suffer big loss in (MA) activity for the ORR (~40 to 60 %) soon after the potential cycling starts (see Fig. S16†).

For a given amount of atomic species in a spherical NP, the surface area that can be associated with the species, usually referred to as a geometric surface area (GSA), is inversely proportional to the diameter, *i.e.* size of the NP. Studies have shown[76,77] that the GSA and ECSA of metallic NPs used as ORR catalysts are strongly related to each other and, hence, changes in the former can be used as a relative measure of changes in the latter. The average size of Pd–Cu alloy NPs functioning at the cathode of the operating PEMFC was determined by analysis of the width of Bragg-like peaks in the respective *in operando* HE-XRD patterns using the Scherrer formalism.[74] As it may be expected,[4,12,17] it was found that the NPs grow in size, that is, their GSA decreases during the PEMFC operation. The evolution of the GSA of Pd–Cu alloy NPs with the number of PEMFC cycles is shown in Fig. S6.† As can be seen in the figure, the GSA, and very likely ECSA, of Pd–Cu alloy NPs decreases gradually to about 90% of its initial value during 1450 potential cycles. In general, losses in GSA are considered detrimental to the ORR activity of NM–TM nanoalloys.[4,12,78–82] Hence, the gradual loss in GSA (ECSA) seen in Fig. S6† would definitely contribute to the total loss in ORR activity suffered by Pd–Au alloy NPs during the PEMFC operation. The likely magnitude of this contribution is discussed below.

Changes in the bonding distances in Pd_xCu_{100-x} alloy NPs ($x = 34$, 51, 75) during the PEMFC operation are summarized in Fig. S7.† The changes reflect the increasing shift in the position of the peaks in the respective *in operando* atomic PDFs towards larger *r*-values with the number of PEMFC cycles (*e.g.* Fig. 2a). As can be seen in Fig. S7,† bonding distances in Pd–Cu alloy NPs tend to approach those in pure Pd (2.76 Å) during the PEMFC operation. In particular, bonding distances in Pd_xCu_{100-x} alloy NPs ($x = 34$, 51, 75) which have undergone 1450 PEMFC cycles increase to 2.65 Å, 2.70 Å and 2.73 Å, *i.e.* by 0.3 Å, 0.3 Å and 0.1 Å, respectively, as compared to those in the fresh NPs. Hence, for reasons discussed above, bonding effects that promote the ORR over Pd–Cu alloy NPs, such as exchange of charge between Cu and Pd atoms and related compressive strain, would weaken during the PEMFC operation. As a result, the ORR activity of Pd–Cu alloy NPs would drop, as indeed observed (compare with data in Fig. S5†). As can also be seen in the figure, changes in the bonding distances in Pd_xCu_{100-x} alloy NPs ($x = 34$, 51, 75) do not scale linearly with the number of PEMFC cycles reminiscent of the concurrent decay of the (MA) ORR activity of the NPs.

Changes in the nanophase composition of Pd_xCu_{100-x} alloy NPs ($x = 34$, 51, 75) during the PEMFC operation were explored by the "search and match" procedure described in the Methods section of the ESI.† The procedure consists of a systematic comparison between *in operando* and nanophase model computed PDFs, as illustrated in Fig. S12–S14.† The results of the "nanophase analysis" indicated that, under operating conditions, the NPs largely preserve their distinct nanophase type (see Fig. 2b), that is, $Pd_{34}Cu_{66}$ and $Pd_{51}Cu_{59}$ NPs remain nanoalloys whose interior and exterior regions are with a bcc- and fcc-type structure whereas $Pd_{75}Cu_{25}$ NPs persists as fcc-type nanoalloys. Also, the results indicated that the surface of cycled NPs is further enriched in Pd species as compared to that of fresh NPs (see Fig. 2a).

To quantify the relationship between the structural changes and loss in ORR activity experienced by Pd_xCu_{100-x} alloy NPs ($x = 34$, 51, 75) during potential cycling inside the PEMFC, experimental data for the GSA, MA for the ORR and phase composition of the NPs were summarized as a function of the number of PEMFC cycles in Fig. 3–5, respectively. Experimental data for the evolution of Pd-involving bonding distances in the NPs and colour maps of the respective *in operando* atomic PDFs are also shown in the figures. As can be seen in the figures, the sharp drop in the ORR activity of the NPs occurring within the first few hundred potential cycles coincide with a sharp decline in the bonding effects in the NPs, as reflected by the fast shift of

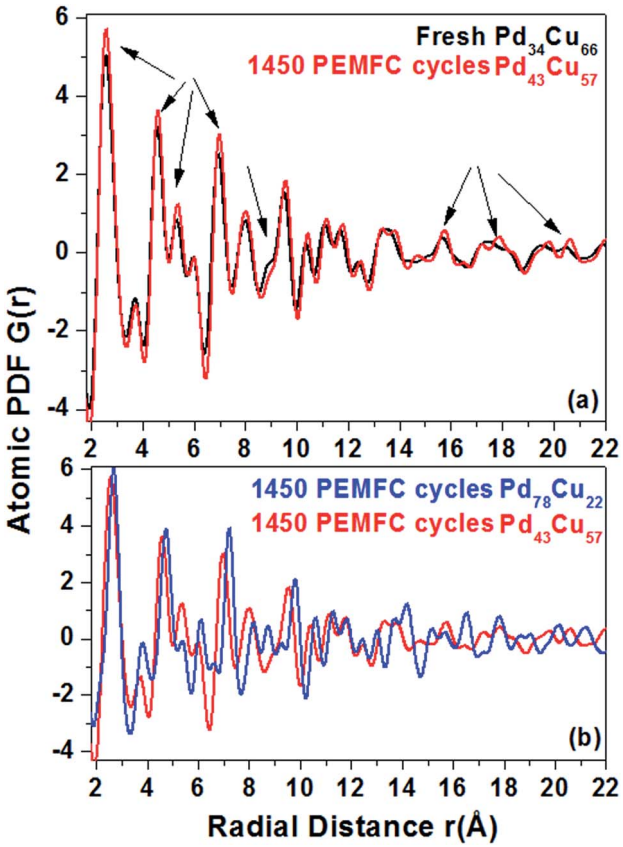

Fig. 2 (a) Experimental atomic PDFs of fresh and cycled $Pd_{34}Cu_{66}$ NPs. The chemical composition of the NPs changes during the cycling to $Pd_{43}Cu_{57}$, as determined by ICP-AES. Accordingly, corresponding peaks in the PDFs of fresh and cycled NPs show differences in intensity and shape (follow the arrows). Besides, peaks in the PDF of cycled $Pd_{34}Cu_{66}$ NPs are systematically shifted to higher-*r* distances. The shift reflects the increase in the bonding distances in cycled $Pd_{34}Cu_{66}$ NPs toward those in pure Pd. (b) Experimental atomic PDFs of $Pd_{34}Cu_{66}$ and $Pd_{75}Cu_{25}$ undergone 1450 potential cycles. The chemical composition of the NPs has changed during the cycling to $Pd_{43}Cu_{57}$ and $Pd_{78}Cu_{22}$, respectively, as determined by ICP-AES. The PDFs are markedly different reflecting the different nanophase state of the NPs. That is, as per the results of nanophase analysis described in the Methods section of the ESI (see Fig. S11–S14†), $Pd_{43}Cu_{57}$ NPs are composed of a bcc core and fcc shell while $Pd_{78}Cu_{22}$ NPs are an fcc Pd–Cu nanoalloy with a surface enriched in Pd. The nanophases are shown in Fig. S8 and S10,† respectively.

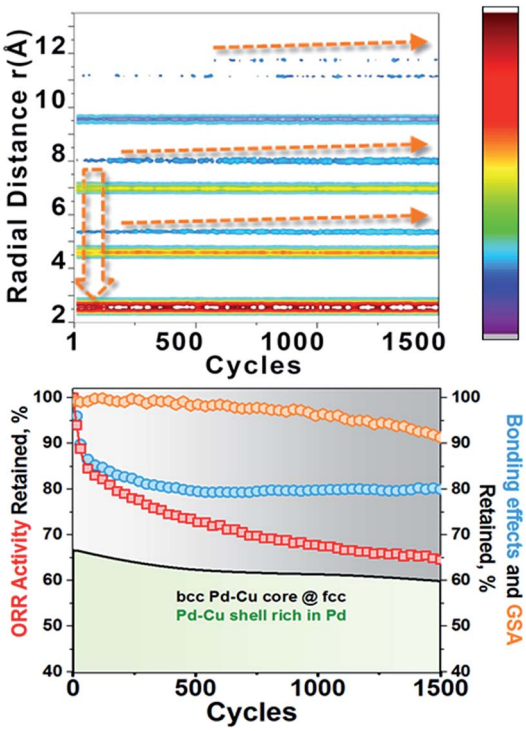

Fig. 3 (Upper panel) Colour map of the low-*r* part of the *in operando* atomic PDFs of $Pd_{34}Cu_{66}$ alloy NPs. Slanted arrows highlight the gradual evolution of PDF features at about 5 Å, 8 Å and 12 Å with the number of potential cycles. Vertical arrow highlights the sudden change in the intensity of several PDF features occurring within the initial 500 potential cycles. The highlighted changes in the experimental PDF data reflect specific structural changes of $Pd_{34}Cu_{66}$ NPs. As discussed in the text, the latter can be related to distinct stages in the evolution of the effective ORR (MA) activity of $Pd_{34}Cu_{66}$ during the PEMFC operation. Note, the intensity of the presented PDF features increases as their colour changes from blue towards red. The increase is at a constant rate indicated by the colour bar on the right. (Lower panel) Rate of retention (in %) of the ORR (MA) activity (red squares) and GSA (orange rhombs) of $Pd_{34}Cu_{66}$ NPs with the number of potential cycles. The relative percentages of the total volume of the NPs occupied by a bcc Pd–Cu core (gray area) and Pd–Cu shell rich in Pd (green area) are determined by "nanophase analysis" as explained in the text. A thick black line tracks the evolution of the percentages with the number of potential cycles. That is, for 1450 potential cycles, the volume fraction of the bcc core increases from 33% to 40% and that of the fcc shell decreases from 67% to 60%. Note that, as per ICP-AES, the overall chemical composition of the NPs changes to $Pd_{43}Cu_{57}$ because of dissolving of Cu species under the corrosive conditions inside the operating PEMFC. The rate of retention (in %) of the bonding (ligand & geometric) effects in the NPs (blue circles) with the number of potential cycles, as reflected by changes in the bonding distances in the NPs, is also shown. Note, for legibility purposes, the vertical axis starts from 40%.

the bonding distance characteristic for the fresh NPs towards those in pure Pd. The observation indicates that the former, *i.e.* the drop in the ORR, is very likely due to the latter, *i.e.* the sharp decline in the bonding effects. The observed correlation between the fast decay of the MA for the ORR and "decompression" of bonding distances experienced by the NPs cycled inside the PEMFC can be rationalized as follows: as per ICP-AES data, Cu atoms leach from Pd–Cu alloy NPs during the PEMFC operation. As soon as the leaching process starts, that is, as soon as the PEMFC starts operating, near-surface Cu and Pd atoms remaining in the NPs would start seeking and forming energetically more favourable local configuration through interdiffusion. As a result, the near-surface region of the NPs would undergo a fast reconstruction because the interdiffusion of atomic species in metallic NPs can be several orders of magnitude faster than that in their bulk counterparts.[83–85] Such a reconstruction would disrupt cooperative interactions between near-surface Pd and Cu atoms in the NPs to a large degree, in particular the bonding (ligand and strain) effects discussed above, and so the atoms would relax towards their elemental state in the respective solid, including a relaxation of

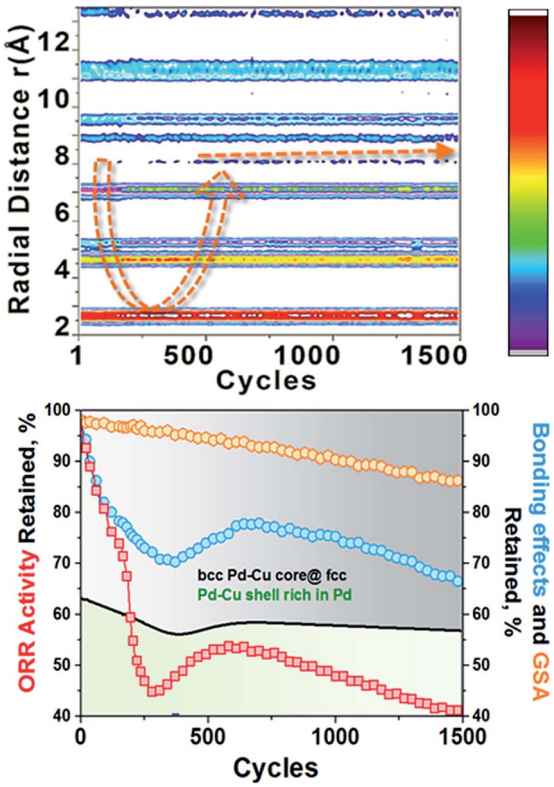

Fig. 4 (Upper panel) Colour map of the low-*r* part of the *in operando* atomic PDFs of $Pd_{51}Cu_{49}$ alloy NPs. U-shaped arrow highlights a slow-mode oscillation of the intensity of several PDF features occurring within the initial 500 cycles. Slanted arrow highlights the gradual evolution of a PDF feature emerged after the initial 500 potential cycles. The highlighted changes in the experimental PDF data reflect specific structural changes of $Pd_{51}Cu_{49}$ NPs. As discussed in the text, the latter can be related to distinct stages in the evolution of the effective ORR (MA) activity of $Pd_{51}Cu_{49}$ NPs during the PEMFC operation. Note, the intensity of the presented PDF features increases as their colour changes from blue towards red. The increase is at a constant rate indicated by the colour bar on the right. (Lower panel) Rate of retention (in %) of the ORR (MA) activity (red squares) and GSA (orange rhombs) of $Pd_{51}Cu_{49}$ NPs with the number of potential cycles. The relative percentages of the total volume of the NPs occupied by a bcc Pd–Cu core (gray area) and fcc Pd–Cu shell rich in Pd (green area) are determined by "nanophase analysis" as explained in the text. A thick black line tracks the evolution of the percentages with the number of potential cycles. That is, for 1450 potential cycles, the volume fraction of the bcc core increases from 38% to 44% and that of the fcc shell diminishes from 63% to 57%. Note that, as per ICP-AES, the overall chemical composition of the NPs changes to $Pd_{61}Cu_{38}$ because of dissolving of Cu species under the corrosive conditions inside the operating PEMFC. The rate of retention (in %) of the bonding (ligand & geometric) effects in the NPs (blue circles) with the number of potential cycles, as reflected by changes in the bonding distances in the NPs, is also shown. Note, for legibility purposes, the vertical axis starts from 40%.

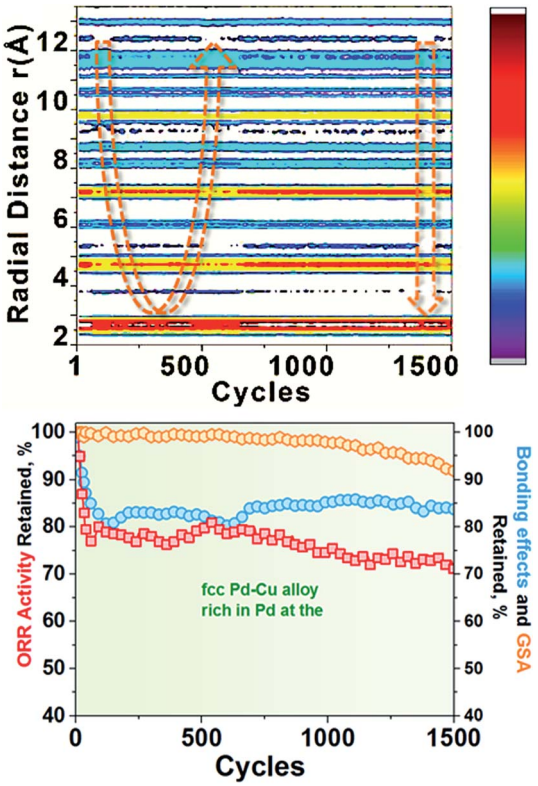

Fig. 5 (Upper panel) Colour map of the low-*r* part of the *in operando* atomic PDFs of $Pd_{75}Cu_{25}$ alloy NPs. U-shaped arrow highlights the sequence of sudden dips and rises of several PDF features occurring within the initial 600 cycles. Vertical arrow highlights a sudden change of several PDF features that occurred after 1300 potential cycles. The highlighted changes in the experimental PDF data reflect specific structural changes of $Pd_{75}Cu_{25}$ NPs. As discussed in the text, the latter can be related to distinct stages in the evolution of the effective ORR (MA) activity of $Pd_{75}Cu_{25}$ NPs during the PEMFC operation. Note, the intensity of the presented PDF features increases as their colour changes from blue towards red. The increase is at a constant rate indicated by the colour bar on the right. (Lower panel) Rate of retention (in %) of the ORR (MA) activity (red squares) and GSA (orange rhombs) of $Pd_{75}Cu_{25}$ NPs with the number of potential cycles. The NPs remain single fcc Pd–Cu nanophase rich in Pd at the surface throughout the cycling. As per ICP-AES though, the overall chemical composition of the NPs changes to $Pd_{78}Cu_{22}$ because of dissolving of Cu species under the corrosive conditions inside the operating PEMFC. The rate of retention (in %) of the bonding (ligand & geometric) effects in the NPs (blue circles) with the number of potential cycles, as reflected by changes in the bonding distances in the NPs, is also shown. Note, for legibility purposes, the vertical axis starts from 40%.

metal-to-metal atom bonding distances. Hence, it may be expected that, due to a weakening of the catalytic synergy between near-surface Cu and Pd atoms triggered by the dissolution of the former, the ORR activity of Pd–Cu alloy NPs would drop soon after they are exposed to the highly corrosive environment inside the operating PEMFC. Furthermore, it may be expected that Pd–Cu alloy NPs suffering a relatively large loss in Cu species during the PEMFC operation, such as $Pd_{51}Cu_{49}$ alloy NPs (Cu loss > 10%), would undergo a relatively large-scale near-surface reconstruction, including a relatively large relaxation of the characteristic for the NPs bonding distances. Thus, the NPs would suffer a relatively large loss in ORR activity as compared to Pd–Cu alloy NPs suffering a relatively small loss of Cu species during the PEMFC operation, such as $Pd_{75}Cu_{25}$ NPs (Cu loss ~ 3%). Indeed, this is exactly what a comparison between data in Fig. 3–5 shows. Note, the observed sharp drop in the ORR activity of Pd_xCu_{100-x} alloy NPs ($x = 34, 51, 75$) may not be due

to a sharp decrease in their GSA\ECSA because, as the analysis of the width of Bragg-like peaks in the *in operando* HE-XRD patterns shows, the growth of the NPs is rather limited during the first few hundred potential cycles inside the PEMFC. As data in Fig. 3–5 indicate though, the gradual growth of Pd–Cu alloy NPs during a prolonged PEMFC operation is likely to become increasingly responsible for the further loss in ORR activity suffered by the NPs as the number of potential cycles approaches 1000, and beyond.

Last but not least, it may be expected that the envisaged interdiffusion of Pd and Cu atoms in Pd_xCu_{100-x} alloy NPs (x = 34, 51, 75) would not be limited to the NP surface alone and, furthermore, would carry on until its major driving force, that is the leaching of Cu species from the NPs, lasts, *i.e.* until the PEMFC operates. This may lead to relatively long-lived (*e.g.* ~1 h) nanophase fluctuations within the NPs, often associated with the so-called "compositional waves",[66,70,73] such as those experienced by $Pd_{51}Cu_{49}$ alloy NPs during the initial 700 potential cycles. Intermittent fluctuations in the bonding effects/distances in the NPs, such as those experienced by $Pd_{75}Cu_{25}$ alloy NPs that have undergone approximately 600 and then a further 700 (1300 in total) PEMFC cycles, are also likely to occur. Both the relatively long-lived and intermittent structural fluctuations would result in proportionate in magnitude dips and rises in the ORR activity of the respective NPs. On the other hand, gradual structural changes of Pd–Cu alloy NPs, such as, for example, a gradual increase in the concentration of surface Pd atoms leading to a gradual change in the relative volume ratio of the bcc core and fcc shell forming the NPs, would render the ORR (MA) activity of the NPs slowly drifting towards lower values. That is because, concurrently, the adsorption energy of O_2 and intermediate O-species onto the NP surface and the number of surface Cu sites necessary for the ORR reaction over the NPs to proceed at a high rate would gradually increase and decrease, respectively, to inapt values.[40,56,61–64] Indeed, as data in Fig. 3–5 show, major changes in the ORR activity, including sudden drops, rises and slow-mode oscillations of its values, and in the structural state of Pd–Cu alloy NPs, including changes in the nanophase composition, GSA and interactions between the constituent atoms as reflected by Pd-involving bonding distances, are highly correlated in both magnitude and timing. The latter are revealed by the evolution of specific features of atomic PDFs obtained by *in operando* HE-XRD (see the arrows running through the colour maps of the respective PDFs). The former is revealed by the evolution of the current output of the PEMFC, as derived from standard polarization curves. Altogether, data in Fig. 3–5 evidence the instant link between the ever-adapting structural state of ORR nanoalloy catalysts inside operating PEMFCs and the performance of the PEMFCs.

Conclusions

The as-prepared Pd–Cu alloy NPs with a composition close to that of Pd_1Cu_1 show high catalytic activity for the ORR. It can be attributed to the fcc-type surface of the NPs that is enriched in Pd and, furthermore, strained by both surface Cu atoms and the bcc-type interior of the NPs. Under actual operating conditions though, the NPs quickly suffer big loss in ORR activity due to a surface reconstruction and the associated weakening of bonding interactions between the constituent atoms. The NPs suffer further loss in ORR activity due to nanophase fluctuations, an increased depletion of Cu at their surface and a gradual growth leading to a decrease in their GSA. The fast weakening of bonding interactions is due to intra-particle diffusion of Pd and Cu atoms triggered by leaching of Cu atoms from the NPs during the PEMFC operation. Eventually, the leaching causes nanophase fluctuations in the NPs and likely exchange of atomic species between individual NPs leading to a sizable NP growth. Coalescing of nearby Pd–Cu NPs though may also contribute to the latter. Hence, further efforts to improve the catalytic functionality of Pd–Cu alloy NPs inside operating PEMFCs should aim at restraining both the inherently fast intra-particle diffusion of Cu and Pd atoms and the mass transport at the cathode side of MEAs. As our present *in operando* and earlier *ex situ* studies show,[33,86] though optimal catalysts for the ORR in the as-prepared state, Pd–Cu alloy NPs with a composition close to Pd_1Cu_1 are less durable inside operating PEMFCs (MA loss ~60% for 1450 potential cycles; see Fig. 4 and S16†) in comparison with Pd–Cu alloy NPs with a composition close to Pd_3Cu_1 (MA loss ~28% for 1450 potential cycles; see Fig. 5). In part, this may be due to the fact that the former comprises two nanophases whereas the latter, though definitely inhomogeneous at atomic level, appears as a monophase fcc-type nanoalloys. Besides, being in a clear majority, Pd species in Pd_3Cu_1 NPs seem to protect the minority Cu species from dissolution to a high degree. Hence, considering our findings, affordability issues and predictions of some DFT studies,[87] we argue that Pd–Cu alloy NPs with a composition close to Pd_2Cu_1, *i.e.* in the composition range from Pd_1Cu_1 to Pd_3Cu_1, may turn optimal as catalysts for the ORR taking place at the cathode of operating PEMFCs. Certainly, approaches based on optimizing the synthesis and post-synthesis treatment, the NP size, doping with a third metal,[88] and others, may also turn fruitful. *In operando* HE-XRD can be an effective tool to guide such efforts.

Acknowledgements

The work for this study was supported by DOE-BES Grant DE-SC0006877. This research used resources of the Advanced Photon Source, a U.S. Department of Energy (DOE) Office of Science User Facility operated for the DOE Office of Science by Argonne National Laboratory under Contract No. DE-AC02-06CH11357.

References

1 J. A. Turner, *Science*, 1999, **285**, 687.
2 M. K. Debe, *Nature*, 2012, **486**, 43.
3 A. Rabis, P. Rodriguez and T. J. Schmidt, *ACS Catal.*, 2012, **2**, 804.
4 H. A. Gasteiger, S. S. Kosta, B. Sompalii and F. T. Wagner, *Appl. Catal., B*, 2005, **56**, 9.

5 M. Janik, C. D. Taylor and M. Newrock, *J. Electrochem. Soc.*, 2009, **156**, B126.
6 V. Stamenkovic, B. S. Mun, M. Arenz, K. J. J. Mayrhofer, C. A. Lucas, G. Wang, P. N. Ross and N. M. Markovic, *Nat. Mater.*, 2007, **6**, 241.
7 J. K. Norskov, J. Rossmeisl, A. Logadottir, L. Lundkvist, J. R. Kitchin, T. Bligaard and H. Jonsson, *J. Phys. Chem. B*, 2004, **108**, 17886.
8 B. Hammer and J. K. Norskov, *Adv. Catal.*, 2007, **45**, 71.
9 D. B. Sepa, M. V. Vojnovich and A. Damijanovich, *Electrochim. Acta*, 1981, **26**, B313.
10 V. Stamenkovic, B. S. Mun, K. J. J. Mayrhofer, P. N. Ross, M. N. Markovic, J. Rossmeisl, J. Greeley and J. K. Nørskov, *Angew. Chem., Int. Ed.*, 2006, **45**, 2897.
11 V. Stamenkovic, B. S. Mun, M. Arenz, K. J. J. Mayrhofer, C. A. Lucas, G. Wang, P. N. Ross and N. M. Markovic, *Nat. Mater.*, 2007, **6**, 241.
12 R. Borup, J. Meyers, B. Pivovar, Y. S. Kim, R. Mukundan, N. Garland, D. Myers, M. Wilson, F. Garzon, D. Wood, P. Zelenay, K. More, K. Stroh, T. Zawodzinski, J. Boncella, J. E. McGrath, M. Inaba, K. Miyatake, M. Hori, K. Ota, Z. Ogumi, S. Miyata, A. Nishikata, Z. Siroma, Y. Uchimoto, K. Yasuda, K.-i. Kimijima and N. Iwashita, *Chem. Rev.*, 2007, **107**, 3904.
13 T. Toda, H. Igarashi and M. Watanabe, *J. Electrochem. Soc.*, 1998, **145**, 4185.
14 B. N. Wanjala, R. Loukrampam, J. Luo, P. N. Njoki, D. Mott and C. J. Zhong, *Phys. Chem.*, 2010, **14**, 17580.
15 J. Greeley, I. E. L. Stephens, A. S. Bondarenko, T. P. Johansson, H. A. Hansen, T. F. Jaramillo, J. Rossmeisl, I. Chorkendorff and J. K. Norskov, *Nat. Chem.*, 2009, **1**, 552.
16 L. Chen, H. Guo, T. Fujita, A. Hirata, W. Zhang, A. Inoue and M. Chen, *Adv. Funct. Mater.*, 2010, **21**, 4364.
17 V. R. Stamenkovic, B. S. Mun, K. J. J. Mayrhofer, P. N. Ross and N. N. Markovic, *J. Am. Chem. Soc.*, 2006, **128**, 8813.
18 W. D. Callister, *Materials Science and Engineering: An Introduction*, John Wiley & Sons, New York, 2007.
19 H. R. Colon-Mercado and B. N. Popov, *J. Power Sources*, 2006, **155**, 253.
20 E. Antolini, J. R. C. Salgado and E. R. Gonzales, *J. Power Sources*, 2006, **16**, 957.
21 P. J. Fereira, G. J. Ia O', Y. Shao-Horn, D. Morgan, R. Makharia, S. Kocha and H. A. Gasteiger, *J. Electrochem. Soc.*, 2005, **152**, A2256.
22 V. Petkov, B. Prasai, S. Shan, Y. Ren, J. Wu, H. Cronk, J. Luo and C. J. Zhong, *Nanoscale*, 2016, **8**, 10749.
23 N. Ishiguro, T. Saida, T. Uruga, O. Sekizawa, K. Nagasawa, K. Nitta, T. Yamamoto, S.-i. Ohkoshi, T. Yokoyama and M. Tada, *Phys. Chem. Chem. Phys.*, 2013, **15**, 18827.
24 L. H. Xin, J. A. Mundy, Z. Liu, R. Cabezas, R. Hovden, L. F. Kourkoutis, J. Zhang, N. P. Sabramanian, R. Makharia, F. T. Wagner and D. A. Muller, *Nano Lett.*, 2012, **12**, 490.
25 Y. Yu, H. L. Xin, R. Hovden, D. Wang, E. D. Rus, J. A. Mundy, D. A. Muller and H. A. Abruna, *Nano Lett.*, 2012, **12**, 4417.
26 S. Chen, H. A. Gasteiger, K. Hayakawa, T. Tada and Y. Shao-Horn, *J. Electrochem. Soc.*, 2010, **1577**, A82.
27 S. Mukerjee, S. Srinivasan, M. P. Soriaga and J. McBreen, *J. Electrochem. Soc.*, 1995, **142**, 1409.
28 K. A. Kuttiyiel, K. Sasaki, D. Su, M. B. Vukmirovic, N. S. Marinkovic and R. R. Adzic, *Electrochim. Acta*, 2013, **110**, 267.
29 C. Y. Du, M. Chen, W. G. Wang and G. P. Yin, *ACS Appl. Mater. Interfaces*, 2011, **3**, 105.
30 H. Zhang, Q. Hao, H. R. Geng and C. X. Xu, *Int. J. Hydrogen Energy*, 2013, **38**, 10029.
31 S. Shan, V. Petkov, L. Yang, J. Luo, Ph. Joseph, D. Mayzel, B. Prasai, L. Wang, M. Engelhard and C. J. Zhong, *J. Am. Chem. Soc.*, 2014, **136**, 7140.
32 F. Fouda-Onana and O. Savadogo, *Electrochim. Acta*, 2009, **54**, 1769.
33 J. Wu, S. Shan, J. Luo, P. Joseph, V. Petkov and C. J. Zhong, *ACS Appl. Mater. Interfaces*, 2015, **7**, 25906.
34 L. Xiong, Y.-X. Huang, X. -Wei Liu, G.-P. Sheng, W.-W. Li and H.-Q. Yu, *Electrochim. Acta*, 2013, **89**, 24.
35 F. Hasche, M. Oezaslan and P. Strasser, *J. Power Sources*, 2011, **196**, 5240.
36 V. S. Sundaram, M. B. de Moraes, J. D. Rodriges and G. G. Kleiman, *J. Phys. F: Met. Phys.*, 1981, **11**, 1151; N. Martensson, R. Nyholm, H. Calen, J. Hedman and B. Johansson, *Phys. Rev. B: Condens. Matter Mater. Phys.*, 1981, **24**, 1725.
37 K. J. Kugai, J. T. Miller, E. B. Fox and C. S. Song, *Appl. Catal., A*, 2016, **528**, 67; V. S. Marakatti, S. C. Sarma, B. Joseph, D. Banerjee and S. C. Peter, *ACS Appl. Mater. Interfaces*, 2017, **9**, 3602.
38 I. A. Abricosov, W. Olovsson and B. Johansson, *Phys. Rev. Lett.*, 2001, **87**, 176403.
39 H. T. Tierney, A. E. Baber, E. Ch and H. Sykes, *J. Phys. Chem.*, 2009, **113**, 7246.
40 W. Tang, L. Zhang and H. Henkelmman, *J. Phys. Chem. Lett.*, 2011, **2**, 1328.
41 C. Wang, D. P. Chen, X. Sang, R. R. Unocic and S. E. Skrabalak, *ACS Nano*, 2016, **10**, 6345.
42 C. Xu, Y. Zhang, L. Wang, L. Xu, X. Bian, H. Ma and Y. i. Ding, *Chem. Mater.*, 2009, **21**, 3110.
43 S. Koh and P. Strasser, *J. Am. Chem. Soc.*, 2007, **129**, 12624.
44 J. L. Fernandez, D. A. Walsh and A. J. Bard, *J. Am. Chem. Soc.*, 2005, **127**, 357.
45 C. A. Rice, P. Urchaga, A. O. Pistono, B. W. McFerrin, B. T. McComb and J. Hu, *J. Electrochem. Soc.*, 2015, **162**, F1175.
46 V. Petkov, *Mater. Today*, 2008, **11**, 28.
47 V. Petkov, B. Prasai, Y. Ren, S. Shan, J. Luo, P. Joseph and C. J. Zhong, *Nanoscale*, 2014, **6**, 10048.
48 N. N. Kariuki, X. Wang, J. R. Mawdsley, M. S. Ferrondon, S. G. Niyogi, J. T. Vaughey and D. J. Meyers, *Chem. Mater.*, 2010, **22**, 4144.
49 X. P. Wang, N. N. Kariuki, J. T. Vaughey, J. Goodpaster, R. Kumar and D. J. Meyers, *J. Electrochem. Soc.*, 2008, **155**, 602.

50 M. Mavrikakis, B. Hammer and J. K. Norskov, *Phys. Rev. Lett.*, 1998, **13**, 2819.
51 P. Strasser, S. Oh, T. Anniyev, G. Greely, K. More, C. Yu, Z. Liu, S. Kaya, D. Nordlund, H. Ogasawara, M. F. Toney and A. Nilsson, *Nat. Chem.*, 2010, **2**, 454.
52 A. Ruban, B. Hammer, P. Stoltze, H. L. Skriver and J. K. Norskov, *J. Mol. Catal. A: Chem.*, 1997, **115**, 421.
53 S. Shan, J. Luo, L. Yang and C. J. Zhong, *Catal.: Sci. Technol.*, 2014, **4**, 3570.
54 F. Maroun, F. Ozanam, O. M. Magnussen and R. J. Behm, *Science*, 2001, **293**, 1811.
55 J. K. Norskov, T. Bigaard, J. Rossmeisl and C. H. Christiansen, *Nat. Chem.*, 2009, **1**, 3746.
56 W. Zhang, S. Shan, J. Luo, A. Fisher, J. F. Chen, C. J. Zhong, J. Zhu and D. J. Cheng, *J. Phys. Chem. C*, 2016, DOI: 10.1021/acs.jpcc.6b10814.
57 F. Fouda-Onana, S. Bah and O. Savadogo, *J. Electroanal. Chem.*, 2009, **636**, 1; H. Winter, P. J. Durham, W. M. Temmerman and G. M. Stocks, *Phys. Rev. B: Condens. Matter Mater. Phys.*, 1986, **33**, 2370.
58 L. Zhang and G. Henkelman, *J. Phys. Chem. C*, 2012, **116**, 20860.
59 M. Ren, Y. Zhou, F. Tao, Z. Zou, D. L. Akins and H. Yang, *J. Phys. Chem.*, 2014, **118**, 12669.
60 A. Balerna, C. Evangelisti, R. Psaro, G. Fusini and A. Carpita, *J. Phys.: Conf. Ser.*, 2016, **712**, 012057.
61 J. L. Fernandez, D. A. Walsh and A. J. Bard, *J. Am. Chem. Soc.*, 2005, **127**, 357365.
62 J. L. Fernandez, V. Raghuveer, A. Manthiram and A. J. Bard, *J. Am. Chem. Soc.*, 2005, **127**, 13100.
63 J. L. Fernandez, J. M. White, Y. Sun, W. J. Tang, G. Henkelman and A. J. Bard, *Langmuir*, 2006, **22**, 10426.
64 Y. X. Wang and P. B. Balbuena, *J. Phys. Chem. B*, 2005, **109**, 18902.
65 L. Pauling, *Proc. Natl. Acad. Sci. U. S. A.*, 1950, **36**, 533.
66 L. Pauling, in *The Nature of the Chemical Bond*, Cornell University Press, Ithaca, NY, 1975.
67 L. Pauling, *Proc. Natl. Acad. Sci. U. S. A.*, 1987, **84**, 4754.
68 T. Rajasekharan and V. Seshubai, *Acta Crystallogr., Sect. A: Found. Crystallogr.*, 2012, **68**, 156.
69 J. R. Kitchin, J. K. Norskov, M. A. Barteau and J. G. Chen, *Phys. Rev. Lett.*, 2004, **93**, 156801.
70 A. Navrotsky, *ChemPhysChem*, 2011, **12**, 2207.
71 B. Prasai, A. R. Wilson, B. J. Wiley, Y. Ren and V. Petkov, *Nanoscale*, 2015, **7**, 17902.
72 A. Moelenbroek, S. Haukka and B. S. Klausen, *J. Phys. Chem. B*, 1998, **102**, 10680.
73 P. R. Subramanian and D. E. Laughlin, in *Binary Alloy Phase Diagrams*, ASM international, Materials Park, OH, 1990.
74 P. K. Klug and L. E. Alexander, in *X-Ray Diffraction Procedures: for Polycrystalline and Amorphous Materials*, Wiley, 1974.
75 C. A. Rice, P. Urchaga, A. O. Pistono, B. W. McFerrin, B. T. McComb and J. Hu, *J. Electrochem. Soc.*, 2015, **162**, F1175, see Fig. 2.
76 E. F. Holby, W. Sheng, Y. Shao-Horn and D. Morgan, *Energy Environ. Sci.*, 2009, **2**, 865.
77 J. A. Gilbert, N. N. Kariuki, R. Subbaraman, A. J. Kropf, M. C. Smith, E. F. Holby, D. Morgan and D. J. Myers, *J. Am. Chem. Soc.*, 2012, **134**, 14823.
78 S. Chen, H. A. Gasteiger, K. Hayakawa, T. Tada and Y. Shao-Horn, *J. Electrochem. Soc.*, 2010, **1577**, A82.
79 Y. Hoshi, T. Yoshida, A. Nishikata and T. Tsuru, *Electrochim. Acta*, 2011, **56**, 5302.
80 S. C. Zignani, E. Antolini and E. Gonzalez, *J. Power Sources*, 2008, **182**, 83.
81 L. H. Xin, J. A. Mundy, Z. Liu, R. Cabezas, R. Hovden, L. F. Kourkoutis, J. Zhang, N. P. Sabramanian, R. Makharia, F. T. Wagner and D. A. Muller, *Nano Lett.*, 2012, **12**, 490.
82 Y. Yu, H. L. Xin, R. Hovden, D. Wang, E. D. Rus, J. A. Mundy, D. A. Muller and H. A. Abruna, *Nano Lett.*, 2012, **12**, 4417.
83 J. Horwath, R. Birringer and H. Gleiter, *Solid State Commun.*, 1987, **62**, 319.
84 D. Marks, *Rep. Prog. Phys.*, 1994, **57**, 603.
85 H. Yasuda and H. Mori, *Phys. Rev. Lett.*, 1992, **69**, 3747.
86 Z. Yin, W. Zhou, Y. Gao, D. Ma, C. J. Kiely and X. Bao, *Chem.–Eur. J.*, 2012, **18**, 4887.
87 F. Fouda-Onana and O. Savadogo, *Electrochim. Acta*, 2009, **54**, 1769.
88 R. N. Singh, *Int. J. Electrochem. Sci.*, 2014, **9**, 5607.